The sensitivity of solsticial pauses to atmospheric ice and dust in the MarsWRF General Circulation Model

Christopher Lee[a,b], Mark I. Richardson[b], Claire. E. Newman[b], Michael A. Mischna[c]

[a] *University of Toronto, Toronto, Canada*
[b] *Aeolis Research, Pasadena, California*
[c] *Jet Propulsion Laboratory, California Institute of Technology, Pasadena, California*

Abstract

Mars exhibits less atmospheric variability at the solstices than it does during periods nearer the equinoxes. Much of this variability in air temperature and dust activity is attributable to a significant decrease in eastward traveling transient wave amplitudes in the lower atmosphere near the solstice. Previous versions of the Mars Weather Research and Forecasting (MarsWRF) model using only dust radiative forcing have reproduced the nature but not the magnitude of this 'solsticial pause' in atmospheric variability. In this paper, we use a version of MarsWRF that includes a fully-interactive dust and water cycle to simulate winter solsticial pauses under a range of dust and water ice conditions. The upgraded model specifically includes a new hybrid binned/two–moment microphysics model that simulates dust, water ice, and cloud condensation nuclei. The scheme tracks mass and number density for the three particle types throughout the atmosphere and allows advection by resolved winds, mixing by unresolved processes, and sedimentation that depends on particle size and density. Ice and dust particles interact with radiation in the atmosphere using a Mie scattering parameterization that

allows for variable particle size and composition. Heterogeneous nucleation and condensation use an adaptive bin size scheme to accurately track the particle size during condensation and sublimation processes. All microphysical processes in the model are calculated within the dynamical timesteps using stability-guaranteed implicit calculations with no sub–timestepping. The impact of the addition of water processes to the model was assessed by comparing simulations with only interactive dust (dry simulations) and ones with a fully-interactive dust and water cycle (wet simulations). In dry simulations with dust storms a solsticial pause occurs in the northern winter with a magnitude (or 'depth') that depends on the opacity of the southern summer dust storms. In wet simulations that include water ice and dust particles, deep solsticial pauses are found in both winter hemispheres. In all simulations that reproduce the solsticial pause, energy and instability analysis suggest that a decrease in baroclinic instability and increase in barotropic energy conversion occurs during the solsticial pause. In dry simulations the decrease in baroclinic instability is caused by increased dust opacity leading to increased thermal static stability. In wet simulations, additional opacity from local cap–edge ice clouds reduces the near surface wind shear and further inhibits baroclinic eddy growth. The wet simulations are in better agreement with observations and tend to support results from other models that include ice cloud radiative effects.
Keywords: Mars, solsticial pause, transient waves, dust storms, ice clouds

1. Introduction

The Martian autumn and winter atmosphere is characterized by a relatively high degree of variability in the periods after the autumnal equinox and before the vernal equinox, but with a distinct transition to much lower variability centered on the winter solstice. This transition in the behavior of the polar atmosphere is associated with a dramatic decrease in the number of high latitude dust storms at solstice, as observed by the Mars Global Surveyor (MGS) Mars Orbiter Camera (MOC) (Wang et al., 2003, 2005, Wang, 2007, Guzewich et al., 2015), and a shift to both lower transient wave amplitudes and longer wavelengths, as observed by the MGS Thermal Emission Spectrometer (TES) (Banfield et al., 2004, Wang et al., 2005).

TES observations from just under three Martian years (1999-2006, MY24-27) are available within a gridded 'reanalysis' dataset (the Mars Analysis Correction Data Assimilation (MACDA) reanalysis (Montabone et al., 2014)) that highlights the 'solsticial pause' in particular detail (Lewis et al., 2016, Wang and Toigo, 2016). The reanalysis dataset is especially useful as it provides a uniform estimate of the global state of the atmosphere that is consistent with the more limited observations. As such, it can provide a clearer basis for analysis and yield more robust diagnostics. Using the reanalysis, Lewis et al. (2016) found a solsticial pause in both winter hemispheres with a stronger solsticial pause during northern winter where temperature variability drops by 50% in the near surface atmosphere, and a pause during southern winter with a similar fractional depth but with smaller absolute values. Wang and Toigo (2016) used the same reanalysis dataset to map the relative stengths of the zonal wavenumber 1 to 3 eastward traveling waves as a function of time during the transition into the pause in the northern hemisphere.

General Circulation Models (GCMs) have been used extensively to study transient waves in the northern autumn and winter atmosphere (Barnes et al., 1993, Collins et al., 1996, Wilson et al., 2002, Kuroda et al., 2007, Kavulich Jr et al., 2013, Wang et al., 2013, Wang and Toigo, 2016), and the response of these waves to moderate and large sized dust storms (Basu et al., 2006, Kuroda et al., 2007, Wang and Toigo, 2016), but with only a secondary focus on the pause itself. Most recently, however, Mulholland et al. (2016) used the UK/LMD Mars GCM with both dust and ice radiative forcing to examine the mechanisms of the pause in detail, highlighting the role of both aerosols in modifying the thermal and wind structure at the soltices and in driving the transition of the dominant wavelegths and the amplitudes of trasient waves.

In this paper, we examine the solsticial pause in simulations of the Mars Weather Research and Forecasting (MarsWRF) GCM (Richardson et al., 2007) using a new dust and water ice microphysics scheme. Two groups of simulations are considered. In the first group ('dry'), dust storms are simulated using a two–moment microphysics scheme and are allowed to develop spontaneously in the GCM within a dry atmosphere with no surface or atmospheric water but freely evolving atmospheric dust simulated by the model. In the second group of simulations ('wet'), water vapour and ice are included, and heterogeneous nucleation and condensation processes are allowed to produce a self consistent dust and water cycle. To examine the strength (or *depth*) of the solsticial pause, we examine three simulations with each of the wet and dry GCMs with different dust and water cycles (driven by different dust lifting and nucleation rates), with the dustiest model regularly exhibiting a type of northern winter dust storm found only infrequently in the observational record, and the wettest model exceeding typical observations of the water content of present day Mars. All of the simulations shown use a fully interactive dust and water ice (when present) scheme allowing realistic feedback, and produce stable simulations over decadal timescales.

In section 2 we review the GCM configuration and describe the new microphysics scheme. In section 3 we describe the analysis method used to extract the diagnostics of solsticial pause depth, Eady growth rates, and atmospheric energy conversions. In section 4 the results of the simulations are presented and the diagnostics calculated, and in section 5 our interpretation of those results are discussed. Finally, in section 6 the summary of the simulations and our conclusions are provided.

2. Model Description

In this study, we use the MarsWRF GCM (Richardson et al., 2007, Toigo et al., 2012), which includes a two–stream correlated–k radiative transfer scheme to treat the interaction of radiation with the atmosphere and surface (Mischna et al., 2012), and the Yonsei University boundary layer scheme that treats vertical mixing of heat, momentum, and tracers (Hong et al., 2006). For this study, we also introduce a modified version of a terrestrial cloud microphysics scheme (Morrison and Gettelman, 2008) that treats microphysical interactions between atmospheric water and dust. In combination with the radiative transfer and boundary layer schemes, the new microphysical scheme in this version of MarsWRF allows for the simulation of self-consistent radiative, dynamical, and microphysical interactions between dust, water, and the thermal and dynamical state of the atmosphere.

2.1. Two–moment dust scheme

Dust is simulated in the model with a fully prognostic two–moment treatment implemented within the framework of the Morrison and Gettelman (2008) microphysics scheme. In the two–moment scheme the dust particle size distribution is tracked using the total mass density Q and the total number density N of the dust at each grid point in the atmosphere. We retain the choice made in Morrison and Gettelman (2008) to use the gamma (Γ) function to describe the family of possible particle size distributions. For the gamma function, the number density, ϕ, is given as a function of particle diameter, D, by

$$\phi\left(D\right) = N_0 D^{\mu} \exp^{-\lambda D}, \tag{1}$$

where N_0 is the 'intercept parameter' and λ is the 'slope parameter'. The spectral shape parameter, μ, determines the shape of the distribution within the gamma distribution family, and is prescribed in the model. Negative values of μ have a shape similar to an exponential decay and can be used to simulate a population with large numbers of small particles and fewer large particles. Positive values of μ have a shape similar to normal or log–normal distributions and imply a particle size distribution with a spread of values around a peak value, and the width of the distribution is related to the value of μ (Morrison and Gettelman (2008) use a value of $\mu = 1$ for their Earth microphysics scheme). Using this model we can give expressions for mass density and number density as

$$
\begin{aligned}
N &= m\left(0\right), && (2)\\
Q &= \frac{\pi\rho}{6} m\left(3\right) && (3)
\end{aligned}
$$

where ρ is the particle density, and $m(p)$ is the pth moment of the gamma distribution calculated as

$$m\left(p\right) = \int_0^\infty D^p \phi(D) = \frac{N_0}{\lambda^{\mu+p+1}} \Gamma\left(\mu + p + 1\right). \tag{4}$$

$\Gamma(n)$ is the integrated gamma function, which obeys the relationship $\Gamma(n + 1) = n\Gamma(n)$, and is finite all real numbers except negative integers n (where the integral diverges). For a fixed value of μ, the values of N, Q, and ρ are sufficient to calculate the values of N_0 and λ as

$$
\begin{aligned}
\lambda &= \left(\frac{\pi\rho N \Gamma(\mu+4)}{6Q\Gamma(\mu+1)}\right)^{\frac{1}{3}}, && (5)\\
N_0 &= N\frac{\lambda}{\Gamma(\mu+1)} && (6)
\end{aligned}
$$

Similarly, the effective radius of the distribution (r_{eff}) can be calculated from λ and μ, and the effective variance (v_{eff}) can be calculated directly from μ as

$$
\begin{aligned}
r_{\text{eff}} &= \frac{m(3)}{2m(2)} = \frac{\mu+3}{2\lambda}, && (7)\\
v_{\text{eff}} &= \frac{1}{\mu+3}, && (8)
\end{aligned}
$$

and the mass and number density can be related using r_{eff} as

$$Q = N\frac{4\pi\rho r_{\text{eff}}^3}{3}\frac{(\mu+2)(\mu+1)}{(\mu+3)^2}. \tag{9}$$

Within the atmosphere, dust is affected by both dynamical and microphysical processes. Dynamical processes, including advection and diffusion, are treated entirely within the two–moment framework by advecting and diffusing Q and N as independent tracers. Sedimentation also occurs in the two–moment framework, with sedimentation velocities calculated for Q and N to appropriately reflect the sedimentation rates of different particle sizes and densities (Morrison and Gettelman, 2008). For a single particle size the sedimentation rate is determined by the Stokes–Cunningham velocity

$$V = \frac{\rho g}{18\eta} D^2 (1 + K(A + Be^{-\frac{E}{K}})), \tag{10}$$

where η is the air viscosity, and $K = \frac{2\lambda_f}{D}$ is the Knudsen number, given the mean free path, λ_f. Values of A, B and E used in the model are 1.25, 0.43, and 0.95, respectively (Kasten, 1968). This sedimentation rate can be integrated over the particle distribution to determine an appropriately weighted mean fall speed of the number density (V_N) and mass density (V_Q),

$$\begin{aligned} V_N &= \frac{1}{N}\int_0^\infty V\phi(D)dD, \qquad (11)\\ &= \frac{\rho g(\mu+1)}{18\eta\lambda}\left(\frac{\mu+2}{\lambda} + 2A\lambda_f + \frac{2B\lambda_f}{\left(1+\frac{E}{2\lambda_f\lambda}\right)^{\mu+2}}\right), \\ V_Q &= \frac{1}{Q}\int_0^\infty V\frac{\pi\rho D^3}{6}\phi(D)dD \qquad (12)\\ &= \frac{\rho g(\mu+4)}{18\eta\lambda}\left(\frac{\mu+5}{\lambda} + 2A\lambda_f + \frac{2B\lambda_f}{\left(1+\frac{E}{2\lambda_f\lambda}\right)^{\mu+5}}\right). \end{aligned}$$

At the surface, dust lifting into the atmosphere is parameterized by two processes. One represents sub–grid scale thermal convective lifting, which is usually ascribed to dust devil vortices, and the other represents lifting by model–resolved wind stress (Newman et al., 2002, Basu et al., 2004, Kahre et al., 2006). The dust is lifted with a fixed effective radius, r_{lifted}. The lifting parameterizations control the mass density lifted and r_{lifted} is used to calculate the number density lifted from equation 9

$$\left.\frac{\partial N}{\partial t}\right|_{\text{lifted}} = \frac{3}{4\pi\rho r_{\text{lifted}}^3}\frac{(\mu+3)^2}{(\mu+2)(\mu+1)}\left.\frac{\partial Q}{\partial t}\right|_{\text{lifted}}. \tag{13}$$

Surface dust is stored as mass only with an assumed effective radius that implies a number density on the surface. In the results discussed here we assume surface dust to be infinitely abundant and uniformly accessible. MarsWRF includes the ability to limit the abundance of dust (Newman and Richardson, 2015) but that option is not enabled here as it is not needed to simulate a generally realistic water ice and dust cycle.

Dust is allowed to interact with radiation through scattering and absorption processes within the MarsWRF correlated–k radiation model (Mischna et al., 2012). To account for variable dust particle sizes, a Mie scattering algorithm is used to calculate the scattering and absorption properties of individual dust particles based on their refractive indices (Wolff and Clancy, 2003). For this calculation we calculate scattering and absorption coefficients for 8192 dust particle radii (from 0.01 microns to 500 microns) and for 138 wavelength bins (from 0.15 to 250 microns). Using this dataset a 'lookup table' of optical properties is generated using a gamma distribution with fixed v_{eff} and calculating the distribution weighted mean properties for a range of r_{eff} values from 0.1 microns to 100 microns. The lookup table generated by this calculation is used within the model to calculate the most appropriate optical properties depending on the effective radius at each grid point. Reference optical properties are also calculated at wavelengths (wavenumbers) of 0.67 microns (14925 cm^{-1}), 9.3 microns (1075 cm^{-1}), and 12.1 microns

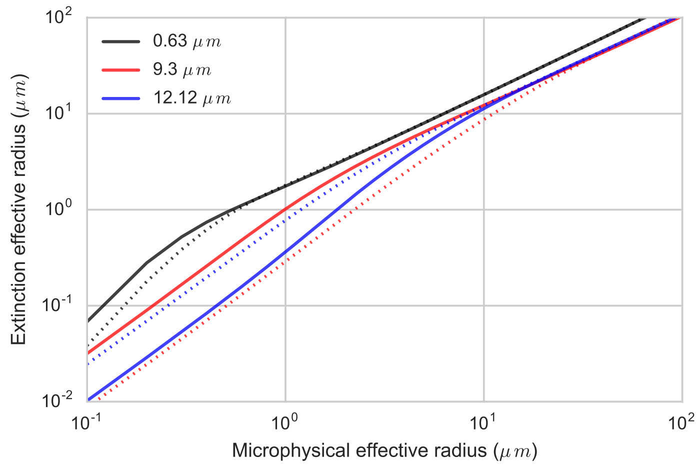

Figure 1: Reference extinction values for $v_{\text{eff}} = 0.25$. Extinction values are shown as the effective radius for radiative processes as a function of the distribution effective radius for microphysics. Solid lines are for dust particles, dotted lines are for water ice particles

(825 cm^{-1}) for diagnostic purposes and comparison with observations from the Mars Global Surveyor (MGS) Thermal Emission Spectrometer (TES). The reference extinction coefficients are shown in Figure 1, plotted as the extinction effective radius $r_{\text{ext}} = \sqrt{\frac{Q_{\text{ext}}}{\pi}}$.

The gamma function requires a value for the variable μ, which defines the effective variance and hence the shape of the gamma function. For dust particles we choose a value of $\mu = 1$, corresponding to $v_{\text{eff}} = 0.25$, which is within the range of v_{eff} values inferred by Wolff et al. (2006) from Mars Exploration Rover observations (0.2–0.8) and by Clancy et al. (2003) based on MGS–TES data (0.1–0.4). Figure 2 shows three distributions using the Gamma function, using a value of $v_{\text{eff}} = 0.25$ (as used here), a value of $v_{\text{eff}} = 0.13$ which would provide a Gamma distribution close to the log–normal

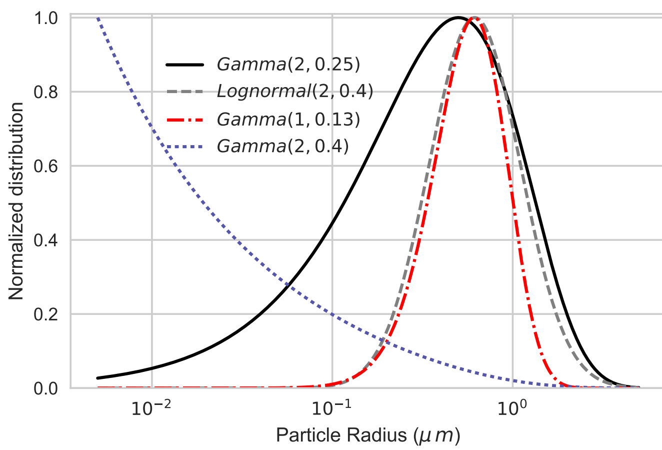

Figure 2: Gamma and log–normal distributions for the effective radius and variance given in the parentheses of each label. (solid black) gamma function with effective radius of $r_{\text{eff}} = 2\mu m$, and effective variance of $v_{\text{eff}} = 0.25$. (dashed grey) Log–normal distribution with $r_{\text{eff}} = 2\mu m$, $v_{\text{eff}} = 0.4$. (dash–dotted red) gamma function with $r_{\text{eff}} = 1\mu m$, $v_{\text{eff}} = 0.13$. (dotted blue) gamma function with $r_{\text{eff}} = 2\mu m$, $v_{\text{eff}} = 0.4$.

distribution used by Madeleine et al. (2011), and a much wider Gamma distribution with negative $\mu = -0.5$ and hence $v_{\text{eff}} = 0.4$. The log–normal distribution from Madeleine et al. (2011) is also shown.

2.2. Water ice model

Water ice and vapor are included in the GCM using the two–moment scheme described above. At the surface, water is stored as ice overlying the surface, and the surface radiative properties are modified (using an emissivity of 1.0 and albedo of 0.33) where there is more than 5 g/m^2 of water. No active regolith water processes are included in the version used in this study. Water ice (vapor) can be sublimated from (condensed onto) the lowest layer depending on the relative humidity of the lowest atmospheric layer and drag speed at the surface interface,

$$\frac{\partial q_{\mathrm{vapor}}}{\partial t} = C_v u^\star (q - q_{\mathrm{sat}}), \tag{14}$$

where q is specific humidity, $u^\star$ is the drag speed at the surface interface, and C_v is a drag coefficient derived from the boundary layer scheme dynamics within the GCM, and depends on the stability conditions in the boundary layer. Similar equations are used to calculate the thermal fluxes at the surface interface.

Once sublimated, water vapor is transported by dynamical processes in the atmosphere, and can nucleate onto bare dust or condense onto ice covered dust. Nucleation follows the parameterization in Inada (2002) and Pruppacher and Klett (2010) assuming direct vapor deposition from a monomer layer of water molecules onto the dust particles (in contrast to the assumptions made in Montmessin et al. (2002) for surface deposition of a steady state influx of water molecules). Condensation follows standard physical parameterizations (Montmessin et al., 2002, Pruppacher and Klett, 2010, Jacobson, 1999) for low concentration volatiles in the Martian atmosphere. In the simulations conducted in this study, the nucleation contact parameter used is $m = 0.95$ unless otherwise specified.

This model differs from prior microphysical models in the calculation of nucleation and condensation by using adaptive particle sizes instead of the more common fixed particle sizes (e.g. Montmessin et al., 2002, Navarro et al., 2014). In our model, the bin locations are specified in terms of quantiles (of fixed percentage) of the total distribution independent of modal radius. These bins remain fixed in percentile space (but move in radius space) as the ice particles grow and shrink and are used by the nucleation and condensation processes to calculate the bin–averaged particle properties such as size, mass, and growth rates. Using fixed quantiles rather than fixed radii means that condensation processes are better resolved at larger particle radius instead of performing most condensation calculations for 'large' particles (e.g. those over 10 microns radius) in a single bin.

During nucleation of water vapor onto bare dust, cloud condensation nuclei (CCN) are formed by scavenging (removing) dust particles from the dust population and tracked as independent particles with additional two–moment mass and number tracers that are transported by atmospheric dynamics. The CCN number tracer becomes the number tracer for ice particles that form on the CCN, and a new mass tracer is used to track the mass of ice deposited onto the CCN population. The radius and mean density of the water ice particles (including contributions of ice and dust) are used in the sedimentation equations 11 and 12 to calculate sedimentation rates for ice particles, allowing the model to properly differentiate ice particles based on radius and mass separately.

All microphysical processes occur on the MarsWRF GCM 'dynamics' timestep (3 minutes for a global 5–degree simulation) with no sub–timestepping in the nucleation or condensation processes. Radiative properties are updated during a 'physics' timestep when radiative flux calculations are performed (typically 15 or 30 minutes for a global 5–degree simulation).

Water ice particles that sediment, or are otherwise transported, to the surface are included in the total ice and dust deposits on the surface. In the current model, dust and ice are separated upon contact with the surface and water ice overlays dust. Surface radiative properties at each grid point are altered if there is sufficient water ice on the surface ($5\,g/m^2$, or equivalently $5.4\,\mu m$ of surface ice depth). Radiative properties of water ice clouds are calculated using the same method applied to dust, using refractive index data for water ice at 220 K (Iwabuchi and Yang, 2011). Reference extinction coefficients used in generating figures for comparison with TES are shown in Figure 1.

In the simulations discussed here, the effective variance (v_{eff}) of the water ice distribution is set to the same value as the dust distribution, with a value of 0.25 (see Figure 2). This choice neglects the narrowing of the water ice distribution by condensation (as assumed by Navarro et al. (2014)) and implies that the mean ice particle age is relatively low and the size distribution of ice particles reflects the size distribution of the CCN.

2.3. Model setup and experiment cases

To examine the solsticial pause with this new model, each simulation uses the self–consistent dust lifting schemes contained in the GCM to produce a dust cycle appropriate for the thermal and lifting conditions in the GCM. Three simulations are performed with the dry GCM: the first has only low opacity background dust (roughly equivalent in average optical depth to the MGS-MCD scenario of Montmessin et al. (2004) but using only interactive dust processes for its generation), the second has a typical unit opacity ($\tau \approx 1$) dust storm, and the third simulation has a larger ($\tau \approx 5$) dust storm (**dryL**, **dryM**, **dryH**, respectively). Three simulations are also performed with the wet GCM: the first has typical northern spring and summer ice cloud abundances and unit optical depth dust storms, the second is a low nucleation rate (contact parameter $m = 0.9$) simulation with higher opacity dust storms and cloud opacities, and the third has a low dust opacity but with water vapor column abundances exceeding those observed on Mars, (**wetL**, **wetM**, **wetH**, respectively). Figure 3 shows the total column opacity at 9.3 microns over the equator for the six simulations used in this paper: By coincidence (rather than by construction) ordering the simulations by peak total opacity is equivalent to ordering the dry models by dust opacity at $L_s = 300°$ (see Figure 4) and the wet models by water ice opacity at $L_s = 150°$ (see Figure 5), but the order of the simulations is not preserved in the depth of the solsticial pause. Figure 4 shows the column dust opacity for these simulations for a year of each simulation. Figure 5 shows the water vapour and ice column abundance for the **wet** models only.

3. Solsticial pause diagnostic

To examine the extent and strength of the solsticial pause we implement a version of the diagnostic developed by Lewis et al. (2016) and Mulholland et al. (2016), where the pause is characterized by the medium–term temperature variability of the winter atmosphere. Specifically, we perform five processing steps: the first two follow Lewis et al. (2016), the third and fourth follow Mulholland et al. (2016) in the generation of a useful metric of pre-solstice and during-solstice atmospheric variability, and finally, we slightly modify a diagnostic developed by Mulholland et al. (2016) that provides a single-valued gauge of the 'depth' of the solsticial pause for a given simulation. Specifically we perform the following calculations:

1. The air temperature on a level 2.5 km above the surface is sampled at

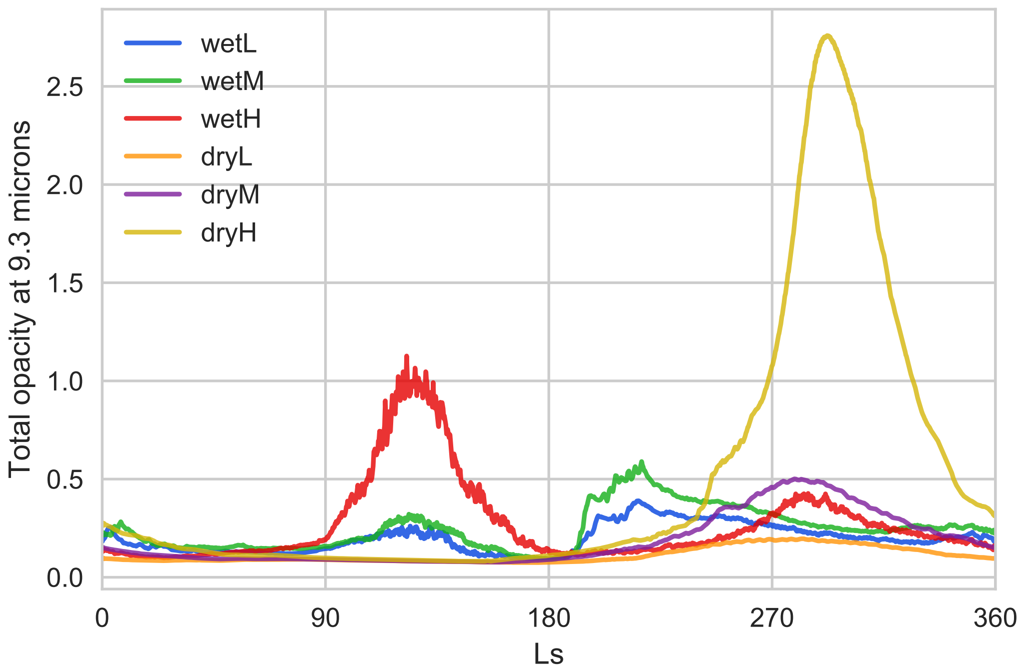

Figure 3: Total column opacity over the equator at 9.3 microns for the six simulations. Data shown in opacity/optical depth units, for the 25th year of each simulation, sampled every 3 hours and averaged into 5–sol periods. The colors used in this figure are used in other figures in this paper to identify the same model where necessary.

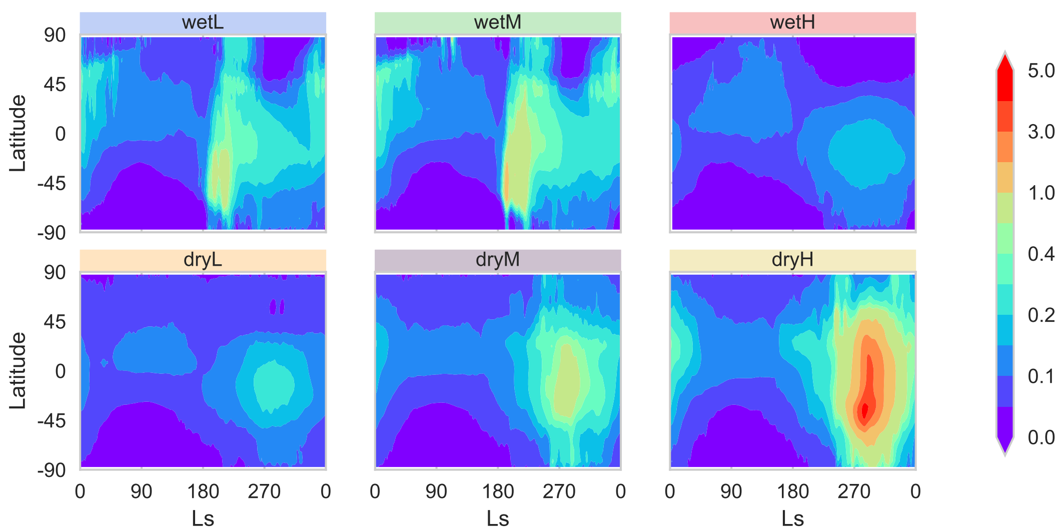

Figure 4: Dust column opacity at 9.3 microns for the six simulations. Wet simulations shown on the top row are (from left to right) **wetL**, **wetM**, **wetH**. Dry simulations are shown on the bottom row (from left to right) **dryL**, **dryM**, **dryH**. Contours shown in opacity units, for the 25th year of each simulation, sampled every 3 hours and averaged into 5 sol periods. The colors used in the sub–plot titles in this figure are used to identify the same simulation in other figures and also correspond to the colors used in the curves in figure 3 and 10.

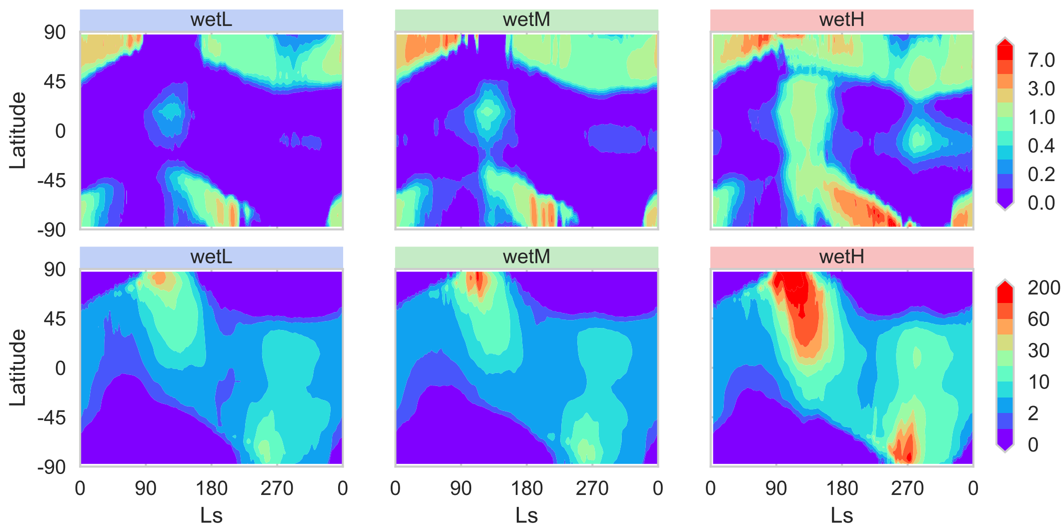

Figure 5: Water ice and vapour for the wet models only. Water ice column opacity at 11.9 microns shown on the top row from simulations (left to right) **wetL**, **wetM**, **wetH**. The bottom row shows water vapour column abundance in precipitable microns for each simulation.

3 hourly intervals and is filtered using a Butterworth (1930) band–pass filter to retain waves with periods of 1.5 to 30 sols. Figure 6 shows an example pressure cycle for this GCM, the Butterworth filter shape as a function of time, and the resulting bandpass filtered dataset.

2. The standard deviation of the filtered temperature is calculated using a 30–sol sliding window, and treated as the atmospheric variability.
3. The domain–maximum value of atmospheric variability is calculated for each time sample in the domain from 30–80° latitude in the winter hemisphere.
4. The time–averaged domain–maximum variability is calculated for two time periods. (A) Within 30° of solstice, and (B) the 180° period surrounding solstice but not including period 'A'. For southern winter region A is $L_s = 60-120°$, region B is $L_s = 0-60°$ and $L_s = 120-180°$. For northern winter region A is $L_s = 240 - 300°$, region B is $L_s = 180 - 240°$ and $L_s = 300 - 360°$.
5. We define the solsticial pause depth as $100\% \times (1 - \frac{A}{B})$ where A and B are the domain averaged values defined above. Larger positive values describe a larger relative decrease in wave activity, *i.e.* a deeper solsticial pause is represented by a larger percentage depth up to a complete cessation of solsticial variance for a depth of 100%. A zero value would suggest no solsticial pause, while negative values describe an increase in wave activity during the solstice. The ratio A/B used by Mulholland et al. (2016) is slightly less intuitive as a gauge of the depth.

For comparison with observations we use the MACDA reanalysis of the MGS TES observations as presented with a specific focus on the solsticial

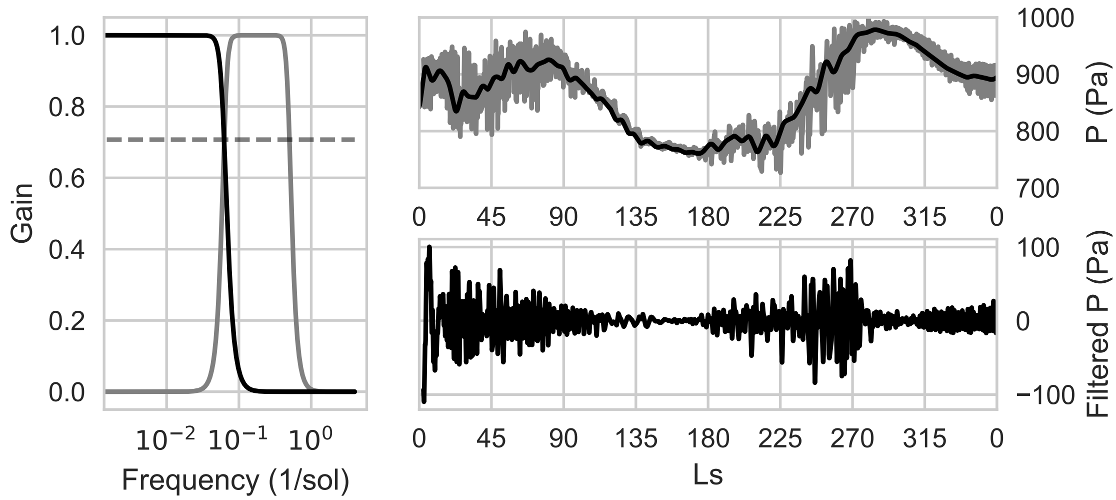

Figure 6: (left) Butterworth band–pass filter (grey) and low–pass filter (black) shown in frequency units. The horizontal dashed line shows the 3 dB drop-off for the filters (where the power would be reduced to 50% of its original value). (top right) Surface pressure data at 70 °N from the **dryM** model (grey) and low–pass filtered data (black) using the low pass filter shown on the left. (bottom right) band-pass filtered pressure data from the same dataset.

pause by Lewis et al. (2016). As in Earth climate studies (e.g. Kalnay et al., 1996) we treat this 'reanalysis dataset' as a proxy for real observational data of the Mars atmosphere. Lewis et al. (2016) provides figures (particularly their figure 1) showing the absolute amplitude of wave activity using similar post–processing methods to those described in this paper. The MACDA reanalysis is also examined by Wang and Toigo (2016), who show the seasonal cycle of the zonal wavenumber 1 to 3 eastward traveling transient waves at low and middle atmospheric levels for the northern hemisphere.

We undertake detailed comparisons with two recent free–run Mars GCM studies of the solsticial pause. Mulholland et al. (2016) use the UK/LMD MGCM with prescribed dust optical depth but an otherwise freely evolving simulation including water ice and dust. The paper provides explicit quantitative diagnostics for their simulations which we reproduce for comparison. Wang and Toigo (2016) use the MarsWRF GCM to perform simulations with highly idealized dust opacity (Montmessin et al., 2004) with ad-hoc wave forcing to induce wavenumber 3 activity during the southern summer dust storms. While they do not explicitly calculate a solsticial pause diagnostic, they do use output from these simulations to calculate the amplitude of waves and energy transfers during the solstice periods.

4. Results

Figure 7 shows the variability of the air temperature at ≈2.5 km altitude for waves with a period of 1.5 to 30 sols for each of the six simulations. This dataset is used to calculate the solsticial pause depth given in Tables 1 and 2. This figure shows a large decrease in northern hemisphere atmospheric variability around $L_s = 270°$ in all wet and two dry models, and a smaller decrease in the dry model with lowest dust opacity (**dryL**). The wet models also have a decrease in the southern hemisphere variability around $L_s = 90°$ while the dry models have a small decrease or increase during the same time period.

For the dry simulations, the depth of the solsticial pause is directly related to the magnitude of the perihelion dust storm, with stronger storms and deeper pauses occurring in the same simulation. The absolute variability (T'_{max}) is also dependent on the dust opacity; higher dust opacity corresponds to lower absolute temperature variability. In the southern winter in these dry simulations, the lack of significant opacity from dust or water ice clouds results in a consistent polar variability across the simulations regardless of peak dust opacity, and with little or no pause in wave activity.

In the wet models the relationship between atmospheric opacity and the solsticial pause depth is similar to the dry models, if we consider the total opacity from the dust and water ice particles. The southern winter pause depth is dependent on the structure and opacity of the polar ice clouds (see Table 2), which varies between the wet simulations. In northern winter the water ice opacity dominates along the edge of the polar night–time (where the solsticial pause is strongest) and is relatively consistent between each simulation as it is controlled more by the presence of water vapor and ice along the polar terminator than the equatorial dust storms. As a result, all three simulations have a pause depth of around 40% and T'_{max} values during northern winter solstice of around 3.5K, both values in agreement with values calculated by Mulholland et al. (2016) for the MACDA reanalysis dataset

(Lewis et al., 2016).

The northern winter solsticial pauses produced in the wet simulations are deeper than the pauses reported in Mulholland et al. (2016), and although Wang and Toigo (2016) do not calculate the same diagnostic, their results are qualitatively comparable to those produced here for the **dryL** simulation. The wet simulations here are closer to the reanalysis results from Lewis et al. (2016) than the free–run simulations from Mulholland et al. (2016). All three wet simulations also have a solsticial pause during the southern winter season (around $L_s = 90°$) along the edge of the southern polar cap instead of the northern cap. The absolute values of T'_{max} found in the wet simulations are in good agreement with the reanalysis dataset shown in figure 1 of Lewis et al. (2016).

4.1. Eady Growth rates

Mulholland et al. (2016) analyzed the solsticial pause in a number of GCM simulations using the UK/LMD GCM that forms the basis of the MACDA reanalysis product (Lewis et al., 2016). In Mulholland et al. (2016), the stability of the atmosphere around winter solstice was studied using the Eady growth rate as a measure of the baroclinic stability of the lower atmosphere. The Eady growth rate (Vallis, 2006) is given by

$$\sigma = 0.31 \frac{f}{N} \frac{\partial \overline{u}}{\partial z} \tag{15}$$

for a Coriolis parameter f, static stability N, and vertical shear of horizontal wind $\frac{\partial \overline{u}}{\partial z}$. High values of σ correspond to large growth rates and a baroclinically unstable atmosphere, making it more likely that baroclinic waves

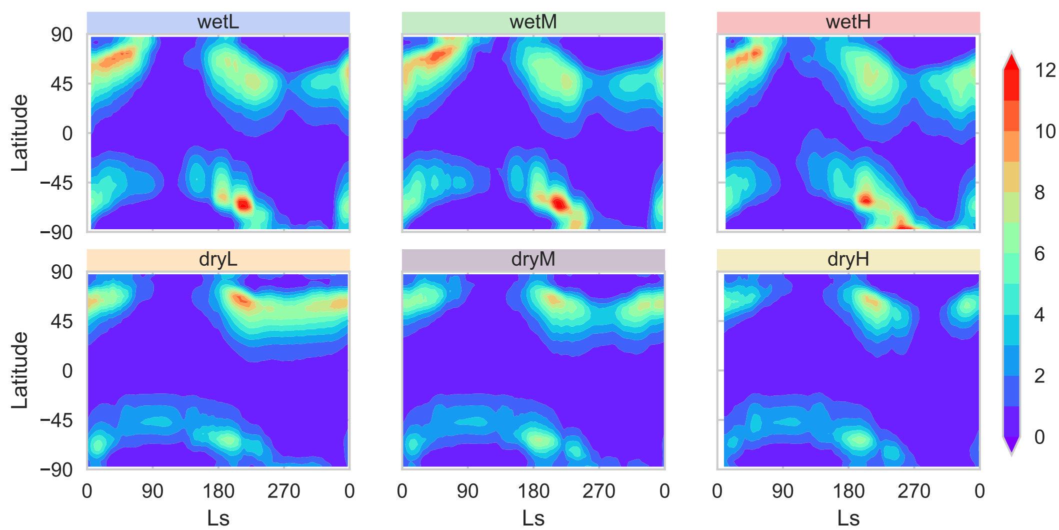

Figure 7: Magnitude of medium–term variability in the lower atmosphere. Calculated as the 30–sol running standard deviation of temperature waves at 2.5km altitude, filtered for waves with periods between 1.5 to 30 sols. Layout as Figure 4, units of K.

Simulation	T'_{max} solstice (K)	T'_{max} surrounding (K)	Pause depth (%)
dryL	6.84	8.32	18
dryM	4.21	6.86	39
dryH	2.14	5.24	59
wetL	3.70	6.07	39
wetM	3.36	5.88	43
wetH	3.55	6.37	44
MACDA	3.35	6.72	50
$\tau_{\mathbf{MY24}}$	6.40	7.09	10
$\tau^{*}_{\mathbf{MY24}}$	5.55	7.94	30
$\tau_{\mathbf{low}}$	7.91	7.42	-7
$\tau^{*}_{\mathbf{low}}$	8.39	9.18	9
$\tau_{\mathbf{high}}$	5.51	7.27	24

Table 1: Average value of meridional domain–maximum ($30° - 80°$ latitude) variability and solsticial pause depth. T'_{max} values are calculated as the seasonal average of meridional maximum standard deviation of 1.5–30 sol period temperature waves at 2.5km altitude, in units of Kelvin. Pause depth in units of percent. The solstice is defined as $L_s = 270° \pm 30°$ and surrounding seasons encompassing $L_s = 180° - 360°$ excluding the solstice period. Top five rows are from the MarsWRF GCM used in this study (see text for simulation label definitions). MACDA values are taken from reanalysis data (Lewis et al., 2016) as presented by Mulholland et al. (2016). Bottom five rows correspond to simulations from the UK/LMD MGCM by Mulholland et al. (2016) using the simulation labels from that paper.

Simulation	$T'_{\max}$ solstice (K)	$T'_{\max}$ surrounding (K)	Pause depth (%)
dryL	3.08	3.50	12
dryM	3.08	3.28	6.3
dryH	3.06	3.04	-0.5
wetL	2.00	3.94	49
wetM	2.49	3.79	34
wetH	1.43	3.85	63

Table 2: As Table 1, but for the southern hemisphere, with solstice defined as $L_s = 90° \pm 30°$ and surrounding seasons encompassing $L_s = 0° - 180°$ excluding the solstice periods.

would be generated, while low values of σ correspond to a more baroclinically stable atmosphere, with eddy generation possibly due to barotropic eddy generation instead (Deng and Mak, 2006). For the free–run simulations and reanalysis dataset in Mulholland et al. (2016) the Eady growth rate was found to decrease during the solsticial pause, a signature of increasing baroclinic stability. Figure 8 shows the value of the Eady growth rate for each simulation in the Northern hemisphere for the half of the Martian year that includes northern winter solstice ($L_s = 180°$–$360°$).

The eddy temperature field in Figure 8 shows the domain–maximum values of the results in Figure 7 (i.e. maximum value between 30°N and 80°N as a function of time) and in each case shows a distinct depression corresponding to the solsticial pause in that simulation. In the dry models, the pause structure is essentially uni–modal, while the dustier wet models have a weak bi–modal structure with a local maximum occurring around $L_s = 315°$. The wet models also appear to have more consistent variability across the simu-

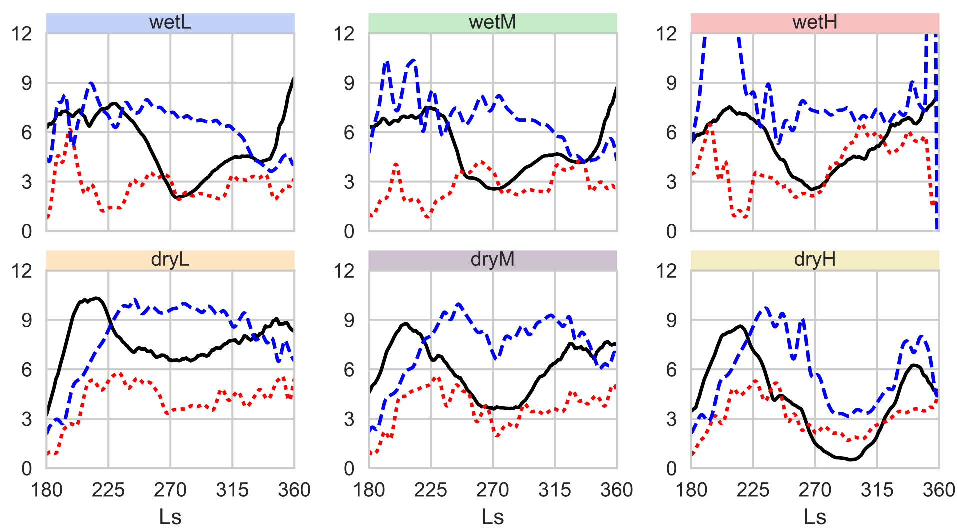

Figure 8: Eady growth rates and eddy temperature fields as a function of L_s for each simulation. Layout as Figure 4. black: Eddy temperature field (K) at 2.5 km altitude, meridional domain maximum at each time. red: Eady growth rate (s^{-1}) at 200 m and at the latitude of maximum eddy temperature (shown in black), blue: meridional domain maximum Eady growth rate (s^{-1}) at 200 m.

lations during the $L_s = 180°$-$225°$ period and consistent timing of minimum variability near Ls=270°. In contrast, the dry models have variation in the amplitude of the maximum variability and timing of the minimum depending on the dust opacity.

In the dry simulations there is a weak correlation between the eddy temperature field and the Eady growth rates at the latitude of the eddy temperature field maximum (i.e. red and black lines). Further, for the **dryL** simulation the domain maximum Eady growth rate (blue line) remains relatively high and lacks a substantial pause. This result is in line with results shown in Mulholland et al. (2016), and suggests that in the dry simulations the observed eddies (in temperature) are influenced by eddies generated further poleward that propagate into the mid-latitudes and maintain the eddy temperature field there.

The wet simulations have no obvious correlation between the Eady growth rates and the temperature field. All three simulations have similar Eady growth rates during solstice and the region of maximum instability in these simulations (where Eady growth rates are maximized) is further removed from the maximum variability, except toward the end of the winter after $L_s = 330°$ where the eddy amplitude peak moves poleward as shown in Figure 12 later.

4.2. Energy transfers

An alternative diagnostic of baroclinic activity was used by Wang and Toigo (2016), who studied wave activity in the MarsWRF GCM using an ad–hoc forcing to simulate a travelling wavenumber 3 mode in the winter atmosphere. Using Fourier decomposition, they found a northern winter solsticial pause and used energy diagnostics to investigate the relative contributions of baroclinic and barotropic processes using the methodology derived in Ulbrich and Speth (1991). In Ulbrich and Speth (1991) the atmosphere is partitioned into four reservoirs (with a further 4 sub–reservoirs not used here) – the mean available potential energy (AZ), eddy available potential energy (AE), mean kinetic energy (KZ), and eddy kinetic energy (KE). The direction and magnitude of energy transfers between these reservoirs can be used as a diagnostic for instability processes in the atmosphere. In particular, baroclinic processes transfer energy along AZ→AE→KE, while barotropic processes transfer energy along AZ→KZ.

Figure 9 shows the calculated energy transfers for the entire year for a region between 50 and 70 degrees north, and 1km to 20km altitude. These plots highlight the different route through which energy is transferred in each simulation. In the dry models, the energy transfer through baroclinic processes (AZ→AE) is relatively consistent throughout the winter, with barotropic processes (AZ→KZ) increasing before solstice and decreasing after it. Increased dust loading corresponds to increased barotropic energy transfer in these simulations, and less consistent baroclinic energy transfer. In the wet models the solsticial pause effect is stronger because of two effects - baroclinic processes (AZ→AE) that dominate away from the solstice rapidly dissipate prior to the solstice, while barotropic processes (AZ→KZ) increase prior to the solstice, as in the dry model. The combination of the two processes produces a more defined pause structure in the wet simulations than in the dry simulations. This difference is also present in the energy reservoirs themselves (not shown): where the dry simulations retain much of the eddy energy (AE

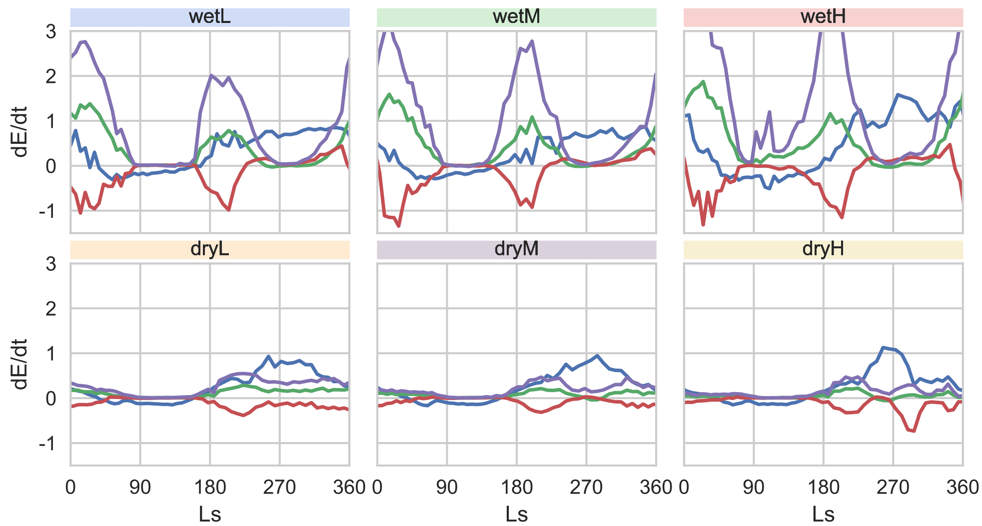

Figure 9: Energy transfer between 50°N and 70°N from 1km to 20km altitude. blue: AZ→KZ, green: AE→KE, red: KZ→KE, magenta: AZ→AE. Units of W/m^2.

and KE) throughout the northern winter, the wet simulations tend to lose eddy energy in favour of zonal mean energy (KZ, in particular).

In the polar region, the transition from baroclinic energy transfers to barotropic energy transfers is driven by a change in the wind and temperature structure in the lower atmosphere, which is partly controlled by the optical depth of aerosols in the atmosphere. Figure 10 shows the vertical gradient of mean horizontal wind and mean temperature profile for the lowest 20km of the atmosphere between 50°N and 70°N, and for periods before, during, and after the solstice. The structural change in the wet simulations occurs as the wind gradients ($\frac{\partial \overline{u}}{\partial z}$) decrease substantially (and almost disappear near the surface) during the pause, reducing the baroclinic growth rate (equation 15). In the dry models, the structural change is more visible in

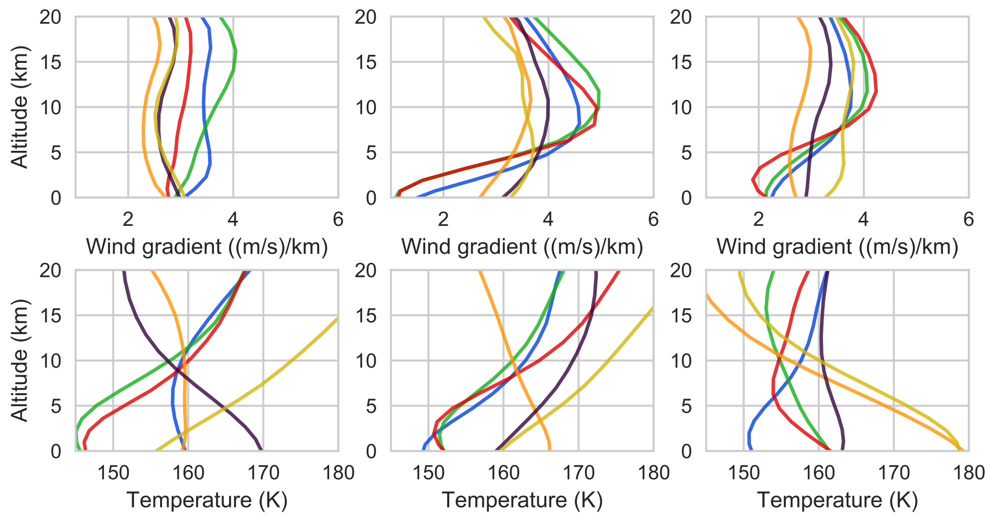

Figure 10: Thermal and wind structure in the lower atmosphere, averaged over $50-70°$N, for the periods (left) $L_s = 210-230°$, (center) $L_s = 260-280°$, (right) $L_s = 310-0°$. (top row) Vertical gradient of zonal (west-east) wind, units of $(m/s)/km$. (bottom row) mean temperature, units of K. orange: **dryL**, purple: **dryM**, yellow: **dryH**, blue: **wetL**, green: **wetM**, red: **wetH**.

the thermal structure, where changes in the temperature profile increase the static stability (N) of the atmosphere and inhibit baroclinic eddy growth.

5. Discussion

From the eddy amplitude plots (Figure 7), it is clear that the pause depth and extent are stronger in simulations with water in the atmosphere than dry simulations, except in simulations with exceptionally large dust storms. In addition, the presence of water greatly stabilizes the northern hemisphere $L_s = 270°$ pause and allows a southern hemisphere $L_s = 90°$ pause to form within the same simulation.

For the $L_s = 270°$ pause, the wet simulations tend to produce a pause amplitude and depth that is relatively insensitive to the dust and water ice abundance and agrees well with the MACDA reanalysis results (Lewis et al., 2016). The wet simulations conducted here are generally in better agreement with the MACDA reanalysis than the the UK/LMD GCM (Mulholland et al., 2016), and, in general, MarsWRF tends to produce deeper solsticial pauses even in dry simulations, as shown here and in Wang et al. (2013) for simpler dust configurations.

The depth of the pause varies between simulations, and has a good correlation with the total opacity near the polar cap edge during the winter solstice. For the northern winter solstice the opacity is provided by a large dust storm in wet and dry simulations, and by ice clouds along the polar terminator in the wet simulations. For the southern winter solstice the dust opacity is consistently low across all simulations and the opacity comes from ice clouds along the equator and along the southern polar terminator (peaking at about 45° latitude in both winter hemispheres). Figure 11 shows the opacity from each aerosol as a function of latitude for 30 degrees around each solstice.

Decomposing the energy reservoirs by longitudinal wavenumber we find that the wet models have a more complex evolution of eddy activity during the northern fall season which might contribute to the enhanced solsticial pause (Figure 12). Wavenumber 1 modes dominate as the polar cap forms, with a transition to higher wavenumber (2–4) modes later in the season before the solsticial pause. After the pause the opposite trend occurs as the ice cap sublimates and polar night retreats poleward. Note that because

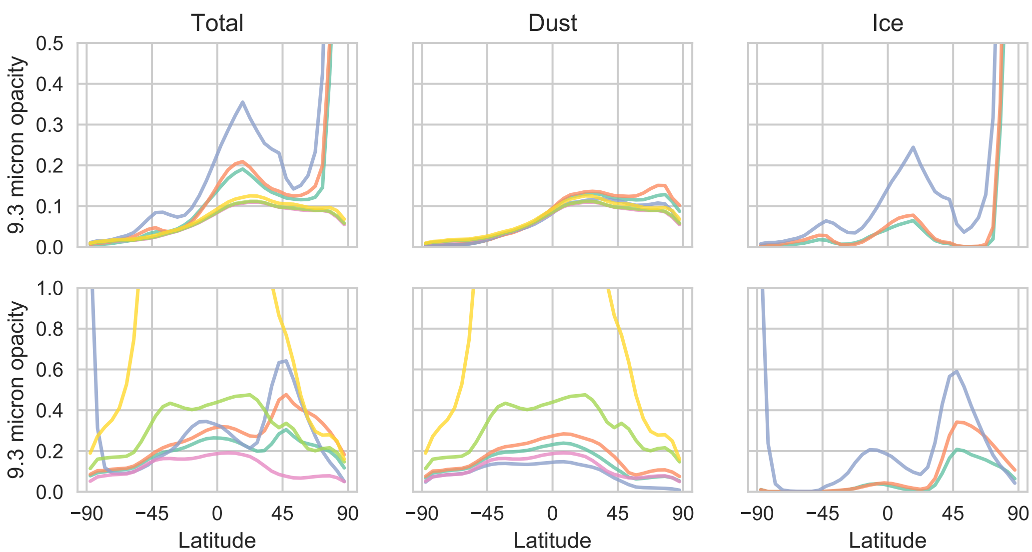

Figure 11: Opacity at 9.3 microns as a function of latitude for 30° of L_s around the southern winter solstice ($L_s = 90°$, top) and the northern winter solstice ($L_s = 270°$, bottom). The plots show (from left to right) the total aerosol opacity, dust opacity, and water ice opacity. As in Figure 3 the colors identify the simulation, wetL (blue), wetM (green), wetH (red), dryL (orange), dryM (purple), dryH (yellow).

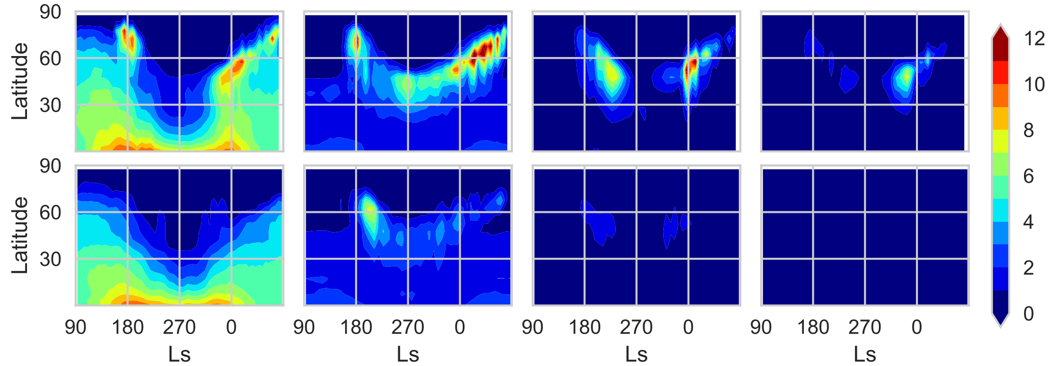

Figure 12: Available Eddy Potential Energy in wavenumber 1–4 (left to right) for wetL (top row) and dryM (bottom) simulations. Contour levels for wavenumber 1 are scaled down by a factor of 2. Units of J/m^2. The horizontal axis has been shifted in these plots to place $L_s = 270°$ at the center of each plot.

MarsWRF is a grid model, the polar points are subject to numerical filtering to ensure stability; however, global wavenumbers 1–4 are not substantially filtered equatorward of 82.5° latitude and do not impact the results here.

In the dry simulations there is an enhancement of the wavenumber 2 mode, but with a distinct lack of energy in the other cap edge modes. This wavenumber 2 mode occurs at the same time and location as the pre–pause enhancement of temperature variability in the dry simulations. In the dustiest dry simulation (**dryH**) there is an additional wavenumber 2 enhancement over the equator during the peak of the storm, which alters the energy balance in the equatorial region and extra–tropics but doesn't contribute significantly to the polar solsticial atmosphere (the oscillation in KZ→KE in **dryH** around $L_s = 300°$ shown in Figure 9 is related to this equatorial enhancement).

As Mulholland et al. (2016) noted, the presence of dust and ice in the atmosphere alters the near–surface thermal structure near the polar cap and reduces the vertical wind shear that drives baroclinic processes in this region. Calculations of baroclinic instability (Mulholland et al., 2016) and energy conversion diagnostics (Wang and Toigo, 2016) tend to suggest that baroclinic energy conversion decreases during solstice and barotropic energy conversion increases to produce the observed pause in eddy activity, in favour of faster zonal mean winds.

6. Conclusions

A new version of the MarsWRF GCM with radiative-dynamical-microphysical feedbacks was used to simulate a range of dust and ice conditions to examine the sensitivity of the solsticial pause. In dry simulations MarsWRF will produce a northern winter solsticial pause if a sufficiently large dust storm is present, but the dust storm peak opacity needed to reproduce the reanalysis results is larger than typically observed on Mars (with peak opacities of 0.5–1), while the pause is observed to occur in the Martian atmosphere during years with and without large dust storms (Lewis et al., 2016). The dry simulations also do not produce a southern summer solsticial pause. In wet simulations MarsWRF produces solsticial pauses in both winter hemispheres, and with a pause depth that is in good agreement with the absolute and relative pause magnitude in the MACDA reanalysis dataset. In all of the simulations conducted, the depth of the solsticial pause is related to the total column aerosol opacity but with a non-linear dependence because of the different spatial and temporal behaviour of dust storms and cap–edge ice clouds. The typical wet simulations (**wetL** and **wetM**) produce solsticial pause depths in both hemispheres that agree well in absolute and relative magnitudes with the MACDA reanalysis.

The solsticial pause occurs in the MarsWRF simulations as baroclinic instabilities that dominate away from the solstice are inhibited during the solstice, allowing an increase in barotropic energy conversion. In dry simulations the inhibition is due to changes in the thermal structure of the lower atmosphere caused by lower latitude dust storms. In wet simulations the inhibition is due to changes in the local opacity due to ice clouds that reduces the near surface wind shear. Both processes lead to a reduction in baroclinic instability growth. The processes generating the pause in MarsWRF with interactive dust and cloud ice are similar to those reported from examination of the MACDA reanalysis data (Lewis et al., 2016), and from previous modeling with the UK/LMD MGCM (Mulholland et al., 2016) and with prescribed dust opacity in MarsWRF (Wang and Toigo, 2016).

The much improved simuation of the solsticial pause with the present version of MarsWRF is due to the addition of a newly developed dust-ice microphysics model. The model uses a hybrid scheme combining efficient two–moment tracers to simulate dynamic processes and accurate adaptive–binned microphysics to simulate nucleation and condensation. Five atmospheric tracers are used to track the evolution of dust mass density, dust number density, water ice mass density, water ice and CCN number density, and CCN mass. The microphysics model allows the radiative forcing of MarsWRF to evolve more realistically as dust and cloud ice abundance and particle size distributions evolve under the influence of interactive dust lifting from the surface, resolved and un-resolved mixing within the atmosphere, microphysical interactions between dust, water, and the atmospheric thermal state, and particle-size-dependent sedimentation. The model results confirm the importance of ice radiative effects for the development of the winter solsticial pause (Mulholland et al., 2016) and for the atmospheric thermal and dynamical state of Mars more generally (Wilson et al., 2007).

Acknowledgement

Funding for this work were provided by the NASA Mars Fundamental Research Program grant NNX13AK67G and the University of Toronto. Resources supporting this work were provided by the NASA High-End Computing (HEC) Program through the NASA Advanced Supercomputing (NAS) Division at Ames Research Center. A portion of this research was carried out at the Jet Propulsion Laboratory, California Institute of Technology, under a contract with the National Aeronautics and Space Administration.

7. References

D. Banfield, B. Conrath, P. Gierasch, R. J. Wilson, and M. Smith. Traveling waves in the martian atmosphere from mgs tes nadir data. *Icarus*, 170(2): 365–403, 2004.

J. R. Barnes, J. B. Pollack, R. M. Haberle, C. B. Leovy, R. W. Zurek, H. Lee, and J. Schaeffer. Mars atmospheric dynamics as simulated by the nasa ames general circulation model: 2. transient baroclinic eddies. *Journal of Geophysical Research: Planets*, 98(E2):3125–3148, 1993.

S. Basu, M. I. Richardson, and R. J. Wilson. Simulation of the Martian dust cycle with the GFDL Mars GCM. *Journal of Geophysical Research*, 109(E11):1–25, 2004. ISSN 0148-0227. doi: 10.1029/2004JE002243. URL `http://www.agu.org/pubs/crossref/2004/2004JE002243.shtml` `http://doi.wiley.com/10.1029/2004JE002243`.

S. Basu, J. Wilson, M. Richardson, and A. Ingersoll. Simulation of spontaneous and variable global dust storms with the GFDL Mars GCM. *Journal of Geophysical Research E: Planets*, 111(9):1–33, 2006. ISSN 01480227. doi: 10.1029/2005JE002660.

S. Butterworth. On the Theory of Filter Amplifiers. *Wireless Engineer*, 7: 536–541, 1930.

R. T. Clancy, M. J. Wolff, and P. R. Christensen. Mars aerosol studies with the MGS TES emission phase function observations: Optical depths, particle sizes, and ice cloud types versus latitude and solar longitude. *Journal of Geophysical Research*, 108

(E9), 2003. ISSN 0148-0227. doi: 10.1029/2003JE002058. URL http://www.agu.org/pubs/crossref/2003/2003JE002058.shtml.

M. Collins, S. Lewis, P. Read, and F. Hourdin. Baroclinic wave transitions in the martian atmosphere. *Icarus*, 120(2):344–357, 1996.

Y. Deng and M. Mak. Nature of the Differences in the Intraseasonal Variability of the Pacific and Atlantic Storm Tracks: A Diagnostic Study. *Journal of the Atmospheric Sciences*, 63(10):2602–2615, 2006. ISSN 0022-4928. doi: 10.1175/JAS3749.1. URL http://journals.ametsoc.org/doi/abs/10.1175/JAS3749.1.

S. D. Guzewich, A. D. Toigo, L. Kulowski, and H. Wang. Mars orbiter camera climatology of textured dust storms. *Icarus*, 258:1–13, 2015.

S. Y. Hong, Y. Noh, and J. Dudhia. A new vertical diffusion package with an explicit treatment of entrainment processes. *Monthly Weather Review*, 134:2318–2341, 2006. URL http://journals.ametsoc.org/doi/abs/10.1175/MWR3199.1.

A. Inada. *Numerical simulations of Martian fog formation and inflight calibration of Mars imaging camera on NOZOMI for its future observations*. PhD thesis, Kobe University, 2002.

H. Iwabuchi and P. Yang. Temperature dependence of ice optical constants: Implications for simulating the single-scattering properties of cold ice clouds. *Journal of Quantitative Spectroscopy and Radiative Transfer*, 112(15):2520–2525, 2011. ISSN 00224073. doi: 10.1016/j.jqsrt.2011.06.017. URL http://dx.doi.org/10.1016/j.jqsrt.2011.06.017.

M. Z. Jacobson. *Fundamentals of Atmospheric Modeling.* Cambridge University Press, 1999.

M. A. Kahre, J. R. Murphy, and R. M. Haberle. Modelling the Martian dust cycle and surface dust reservoirs with the NASA Ames general circulation model. *Journal of Geophysical Research E: Planets*, 111(6):1–25, 2006. ISSN 01480227. doi: 10.1029/2005JE002588.

E. Kalnay, M. Kanamitsu, R. Kistler, W. Collins, D. Deaven, L. Gandin, M. Iredell, S. Saha, G. White, J. Woollen, Y. Zhu, A. Leetmaa, R. Reynolds, M. Chelliah, W. Ebisuzaki, W. Higgins, J. Janowiak, K. C. Mo, C. Ropelewski, J. Wang, R. Jenne, and D. Joseph. The NCEP/NCAR 40-Year Reanalysis Project. *Bulletin of the American Meteorological Society*, 77(3):437–471, mar 1996. ISSN 0003-0007. doi: 10.1175/1520-0477(1996)077¡0437:TNYRP¿2.0.CO;2.

F. Kasten. Falling Speed of Aerosol Particles. *Journal of Applied Meteorology*, 7:944–947, 1968. ISSN 0894-8763.

M. J. Kavulich Jr, I. Szunyogh, G. Gyarmati, and R. J. Wilson. Local dynamics of baroclinic waves in the martian atmosphere. *Journal of the Atmospheric Sciences*, 70(11):3415–3447, 2013.

T. Kuroda, A. S. Medvedev, P. Hartogh, and M. Takahashi. Seasonal changes of the baroclinic wave activity in the northern hemisphere of mars simulated with a gcm. *Geophysical research letters*, 34(9), 2007.

S. R. Lewis, D. P. Mulholland, P. L. Read, L. Montabone, R. J. Wilson, and M. D. Smith. The solsticial pause on

Mars: 1. A planetary wave reanalysis. *Icarus*, 264:456–464, 2016. ISSN 10902643. doi: 10.1016/j.icarus.2015.08.039. URL http://dx.doi.org/10.1016/j.icarus.2015.08.039.

J. B. Madeleine, F. Forget, E. Millour, L. Montabone, and M. J. Wolff. Revisiting the radiative impact of dust on Mars using the LMD Global Climate Model. *Journal of Geophysical Research E: Planets*, 116(11):1–13, 2011. ISSN 01480227. doi: 10.1029/2011JE003855.

M. A. Mischna, C. Lee, and M. I. Richardson. Development of a fast, accurate radiative transfer model for the Martian atmosphere, past and present. *Journal of Geophysical Research*, 117(E10):E10009, oct 2012. ISSN 0148-0227. doi: 10.1029/2012JE004110.

L. Montabone, K. Marsh, S. Lewis, P. Read, M. Smith, J. Holmes, A. Spiga, D. Lowe, and A. Pamment. The mars analysis correction data assimilation (macda) dataset v1. 0. *Geoscience Data Journal*, 1(2):129–139, 2014.

F. Montmessin, P. Rannou, and M. Cabine. New insights into Martian dust distribution and water-ice cloud microphysics. *Journal of Geophysical Research*, 107(E6):5037, 2002. ISSN 0148-0227. doi: 10.1029/2001JE001520. URL http://doi.wiley.com/10.1029/2001JE001520.

F. Montmessin, F. Forget, P. Rannou, M. Cabane, and R. M. Haberle. Origin and role of water ice clouds in the Martian water cycle as inferred from a general circulation model. *Journal of Geophysical Research*, 109 (E10):1–26, 2004. ISSN 0148-0227. doi: 10.1029/2004JE002284. URL http://www.agu.org/pubs/crossref/2004/2004JE002284.shtml.

H. Morrison and A. Gettelman. A new two-moment bulk stratiform cloud microphysics scheme in the community atmosphere model, version 3 (CAM3). Part I: Description and numerical tests. *Journal of Climate*, 21(15):3642–3659, 2008. ISSN 08948755. doi: 10.1175/2008JCLI2105.1.

D. P. Mulholland, S. R. Lewis, P. L. Read, J. B. Madeleine, and F. Forget. The solsticial pause on Mars: 2 modelling and investigation of causes. *Icarus*, 264:465–477, 2016. ISSN 10902643. doi: 10.1016/j.icarus.2015.08.038. URL `http://dx.doi.org/10.1016/j.icarus.2015.08.038`.

T. Navarro, J.-B. Madeleine, F. Forget, A. Spiga, E. Millour, F. Montmessin, and A. Määttänen. Global climate modeling of the Martian water cycle with improved microphysics and radiatively active water ice clouds. *Journal of Geophysical Research: Planets*, 119(7):1479–1495, jul 2014. ISSN 21699097. doi: 10.1002/2013JE004550. URL `http://arxiv.org/pdf/1310.1010.pdf` `http://doi.wiley.com/10.1002/2013JE004550`.

C. E. Newman and M. I. Richardson. The impact of surface dust source exhaustion on the martian dust cycle, dust storms and interannual variability, as simulated by the MarsWRF General Circulation Model. *Icarus*, 257:47–87, 2015. ISSN 10902643. doi: 10.1016/j.icarus.2015.03.030. URL `http://dx.doi.org/10.1016/j.icarus.2015.03.030`.

C. E. Newman, S. R. Lewis, P. P. L. Read, and F. F. Forget. Modeling the Martian dust cycle, 1. Representations of dust transport processes. *Journal of Geophysical Research*, 107

(E12):5123, 2002. ISSN 0148-0227. doi: 10.1029/2002JE001910. URL http://doi.wiley.com/10.1029/2002JE001910 http://oro.open.ac.uk/4504/.

H. R. Pruppacher and J. D. Klett. *Microphysics of Clouds and Precipitation*. Springer, 2010.

M. I. Richardson, A. D. Toigo, and C. E. Newman. PlanetWRF: A general purpose, local to global numerical model for planetary atmospheric and climate dynamics. *Journal of Geophysical Research*, 112(E9): 1–29, sep 2007. ISSN 0148-0227. doi: 10.1029/2006JE002825. URL http://www.agu.org/pubs/crossref/2007/2006JE002825.shtml.

A. D. Toigo, C. Lee, C. E. Newman, and M. I. Richardson. The impact of resolution on the dynamics of the martian global atmosphere: Varying resolution studies with the MarsWRF GCM. *Icarus*, 221(1): 276–288, sep 2012. ISSN 00191035. doi: 10.1016/j.icarus.2012.07.020. URL http://linkinghub.elsevier.com/retrieve/pii/S0019103512002965.

U. Ulbrich and P. Speth. The global energy cycle of stationary and transient atmospheric waves: Results from ECMWF analyses. *Meteorology and Atmospheric Physics*, 45(3-4):125–138, 1991. ISSN 01777971. doi: 10.1007/BF01029650.

G. K. Vallis. *Atmospheric and Oceanic Fluid Dynamics*. Cambridge University Press, 2006.

H. Wang. Dust storms originating in the northern hemisphere during the third mapping year of mars global surveyor. *Icarus*, 189(2):325–343, 2007.

H. Wang and A. D. Toigo. The variability, structure and energy conversion of the northern hemisphere traveling waves simulated in a mars general circulation model. *Icarus*, 271:207–221, 2016.

H. Wang, M. I. Richardson, R. J. Wilson, A. P. Ingersoll, A. D. Toigo, and R. W. Zurek. Cyclones, tides, and the origin of a cross-equatorial dust storm on mars. *Geophysical Research Letters*, 30(9), 2003.

H. Wang, R. W. Zurek, and M. I. Richardson. Relationship between frontal dust storms and transient eddy activity in the northern hemisphere of mars as observed by mars global surveyor. *Journal of Geophysical Research: Planets*, 110(E7), 2005.

H. Wang, M. I. Richardson, A. D. Toigo, and C. E. Newman. Zonal wavenumber three traveling waves in the northern hemisphere of Mars simulated with a general circulation model. *Icarus*, 223(2):654–676, 2013. ISSN 00191035. doi: 10.1016/j.icarus.2013.01.004. URL `http://dx.doi.org/10.1016/j.icarus.2013.01.004`.

R. J. Wilson, D. Banfield, B. J. Conrath, and M. D. Smith. Traveling waves in the Northern Hemisphere of Mars. *Geophysical Research Letters*, 29(14):3–6, 2002. ISSN 0094-8276. doi: 10.1029/2002GL014866. URL `http://www.agu.org/pubs/crossref/2002/2002GL014866.shtml`.

R. J. Wilson, G. A. Neumann, and M. D. Smith. Diurnal variation and radiative influence of martian water ice clouds. *Geophysical research letters*, 34(2), 2007.

M. J. Wolff and R. T. Clancy. Constraints on the size of Martian aerosols from Thermal Emission Spectrometer observations. *Journal of Geophysical Research*, 108(E9):5097, 2003. ISSN 0148-0227. doi: 10.1029/2003JE002057. URL http://doi.wiley.com/10.1029/2003JE002057.

M. J. Wolff, M. D. Smith, R. T. Clancy, N. Spanovich, B. A. Whitney, M. T. Lemmon, J. L. Bandfield, D. Banfield, A. Ghosh, G. Landis, P. R. Christensen, J. F. Bell, and S. W. Squyres. Constraints on dust aerosols from the Mars Exploration Rovers using MGS overflights and Mini-TES. *Journal of Geophysical Research E: Planets*, 111(12):1–23, 2006. ISSN 01480227. doi: 10.1029/2006JE002786.